

# Unexpected activity of MgO nanoclusters for the reductive-coupling synthesis of organonitrogen chemicals with C = N bonds

Received: 12 August 2024

Accepted: 14 March 2025

Published online: 26 March 2025

Ziliang Yuan<sup>1,4</sup>, Bo Han<sup>2,4</sup>, Bing Liu<sup>1,4</sup>, Jie Sun<sup>1</sup>✉, Peng Zhou<sup>1</sup>,  
Rentao Mu<sup>3</sup>✉ & Zehui Zhang<sup>1</sup>✉

Reductive-coupling of nitro compounds and alcohols is a sustainable route for constructing C = N bonds in organonitrogen chemicals, yet challenging due to the inertness of  $\alpha$ -C<sub>sp3</sub>-H bond in alcohols and the vulnerability of C = N bonds towards hydrogenation. Here, we report the surprising catalytic activity of ultrafine alkaline-earth metal oxide MgO nanoclusters ( $0.9 \pm 0.3$  nm) that efficiently activate  $\alpha$ -C<sub>sp3</sub>-H bonds, facilitating the transfer hydrogenation and synthesis of value-added chemicals bearing C = N bonds with high to excellent yields (86–99%). Controlled experiments and characterizations showed the crucial role of oxygen vacancies (O<sub>v</sub>) and local Mg environment (Mg-O bond) in MgO for substrate adsorption and activation via electronic interactions between substrate's negatively charged oxygen atoms and O<sub>v</sub> sites in MgO nanoclusters. Theoretical calculation further confirmed that O<sub>v</sub> significantly lowered the energy barrier of the hydrogen atom transfer from  $\alpha$ -C<sub>sp3</sub>-H in ethanol to the nitro group in nitrobenzene (29.3 *vs.* 52.9 kcal/mol), which is the rate-determining step with the highest energy barrier in reductive-coupling reactions. Our method not only provides an efficient and sustainable pathway for synthesizing organonitrogen chemicals with C = N bonds but also inspires the exploration of main group element catalysts as alternatives to transition metal and noble metal catalysts for organic transformations.

Selective construction of unsaturated C = N bonds is highly important in chemistry as well as biology, as the organonitrogen chemicals such as imines and *N*-heterocycles with C = N bonds are widely present in many fields such as fine chemicals, material science, pharmaceutical research, molecular motors, dye and pigment industry<sup>1–4</sup>. Generally, the construction of C = N bonds can be selectively achieved under oxidative or inert atmospheres. For example, the coupling of aldehydes or ketones with amines is a simple way to build C = N bonds. Substrates for the construction of C = N bonds under an oxidative or inert atmosphere are limited to amines<sup>5,6</sup>. Compared with amines, nitro

compounds are more attractive for the one-pot synthesis of organonitrogen chemicals with C = N bonds under reductive conditions, avoiding the hydrogenation of nitro compounds into amines and the purification of amines<sup>2,7–9</sup>. However, it is challenging to selectively attain the C = N bonds under reductive conditions, because C = N bonds are highly likely to be hydrogenated into C-N bonds (Fig. 1A)<sup>6–11</sup>.

Recently, reductive-coupling of nitro compounds with alcohols represents one of the most promising and sustainable routes for the synthesis of organonitrogen chemicals<sup>2,7–11</sup>. On the one hand, alcohols are readily available at low cost either from fossil resources or

<sup>1</sup>Key Laboratory of Catalysis and Energy Materials Chemistry of Ministry of Education, College of Chemistry and Material Sciences, South-Central Minzu University, Wuhan 430074, P. R. China. <sup>2</sup>Sustainable Energy Laboratory, Faculty of Materials Science and Chemistry, China University of Geosciences, Wuhan 430074, P. R. China. <sup>3</sup>State Key Laboratory of Catalysis, Dalian Institute of Chemical Physics, Chinese Academy of Sciences, Dalian 116023, P. R. China. <sup>4</sup>These authors contributed equally: Ziliang Yuan, Bo Han, Bing Liu. ✉e-mail: [jetsun@mail.scuec.edu.cn](mailto:jetsun@mail.scuec.edu.cn); [murt@dicp.ac.cn](mailto:murt@dicp.ac.cn); [zehuizh@mail.ustc.edu.cn](mailto:zehuizh@mail.ustc.edu.cn)

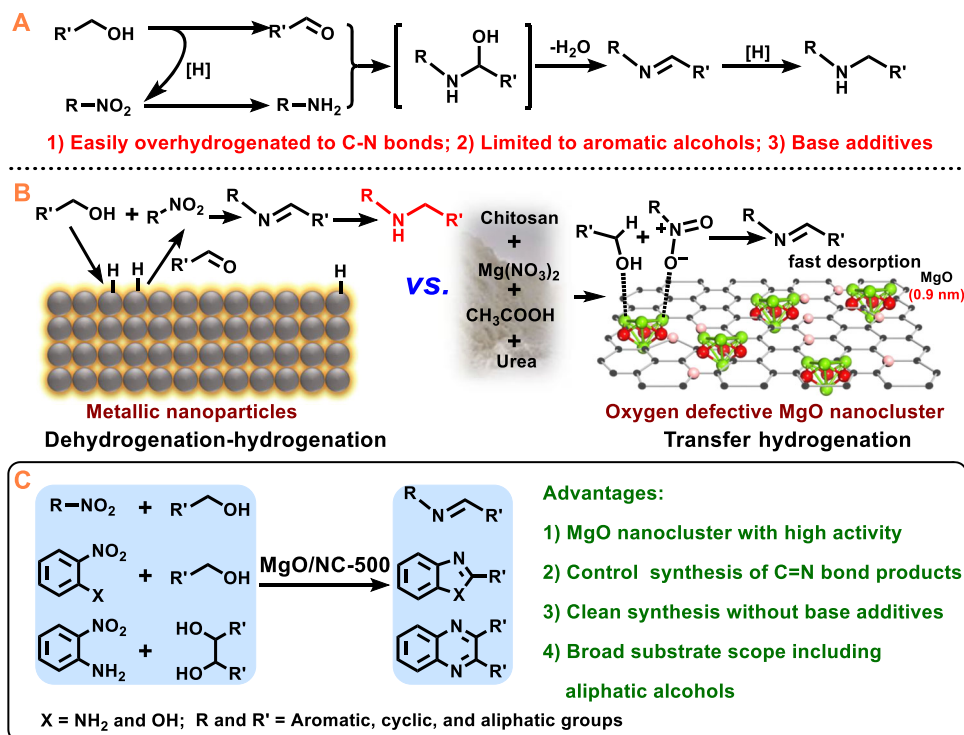


**Fig. 1 | Current methods for the reductive-coupling of nitro compounds and alcohols. A** Reductive-coupling of nitro compounds and alcohols; **B** Regulating the selectivity to C=N bonds by oxygen defects; **C** Application.

renewable biomass. On the other hand, the use of alcohols as the coupling reagents does not require the use of H<sub>2</sub> or other hydrogen donors<sup>12–14</sup>. As a matter of fact, the reductive-coupling of nitro compounds with alcohols has been extensively studied in recent years, but secondary amines with C-N bonds were produced in most cases (Fig. 1B, left)<sup>7,10,15–17</sup>. There are only a few cases of the successful synthesis of imines with C=N bonds via reductive-coupling strategy, and most of them involved noble metal catalysts<sup>7,15</sup>. Furthermore, the current reductive-coupling methods are limited to active aromatic alcohols in the presence of base additives. Therefore, the design of new catalytic systems for the selective synthesis of organonitrogen chemicals with C=N bonds, especially those based on non-noble metal catalysts with low cost, facile preparation procedure, high activity without adding external bases, and broad substrate scope, is highly significant both in academic research and industrial applications.

Some transition metal oxides have been discovered to be effective alternatives to transition metal nanoparticles in catalysis<sup>18–22</sup>. These transition metal oxides, such as molybdenum oxides and cerium oxides, generally have flexible valence states to mediate the redox reactions<sup>19,20</sup>. Nonreducible metal oxides (such as MgO and Al<sub>2</sub>O<sub>3</sub>) are believed to be inactive for the redox reactions, which are only used as the acid-base catalysts or supports to load metal nanoparticles<sup>23,24</sup>, single metal atoms<sup>25,26</sup> or organometallic chemistry species<sup>27,28</sup>. It would be promising and exciting to use the earth-abundant and non-toxic main group metal oxides for redox reactions<sup>29,30</sup>. In recent years, the preparation of small-sized nanoparticles<sup>31,32</sup>, the creation of metal oxides with oxygen vacancies (denoted as O<sub>v</sub>)<sup>33,34</sup> and under-coordinated sites<sup>35,36</sup> were proved to be effective ways for enhancing the reactivity of nonreducible metal oxides by creating reducible surface sites. For example, Huang and co-workers have demonstrated that ultrasmall zirconia nanoparticles, covalently embedded in silica and clamped in a void between two mesoporous platelets, are highly active in the hydrogenolysis of polyethylene<sup>32</sup>. The architecture enhances the catalytic activity of zirconia to become comparable to that of Pt/C and improves its selectivity towards liquid products. As mentioned above,

the reductive-coupling of nitro compounds and alcohols generally requires the use of base additives. Considering the fact that MgO is a strong solid base, it is anticipated that small-sized MgO nanoparticles with abundant O<sub>v</sub> and undercoordinated sites would be effective for the reductive-coupling of nitro compounds with alcohols for the synthesis of organonitrogen chemicals (Fig. 1B, right). Moreover, the different reaction mechanisms of small-sized MgO nanoparticles, as compared with that of conventional metallic nanoparticles, would also be suitable for the construction of C=N bonds. However, it is difficult to get small-sized MgO with a high dispersion and high stability.

Our group and other researchers have recently discovered that nitrogen-doped carbon materials could effectively stabilize small-sized metal nanoparticles, metal nanoclusters, as well as single metal atoms<sup>37–39</sup>. Herein, nitrogen-doped carbon supported defective MgO nanoclusters were successfully prepared by calcining chitosan coordinated Mg<sup>2+</sup> under N<sub>2</sub> atmosphere. The nitrogen-doped carbon supported defective MgO nanoclusters showed high catalytic activity for the reductive-coupling of nitro compounds with alcohols towards the synthesis of imines and N-heterocycles with C=N bonds (Fig. 1C). MgO nanoclusters with O<sub>v</sub> and unsaturated Mg<sup>2+</sup> facilitated the activation of substrates as well as the hydrogen transfer reactions and also guaranteed the selectivity of imines and N-heterocycles with C=N bonds.

## Results

### Catalyst preparation and characterization

Nitrogen-doped carbon supported MgO catalysts were prepared according to the procedure as illustrated in Fig. 2A. A Mg<sup>2+</sup>-containing sol-gel was first prepared by mixing Mg(NO<sub>3</sub>)<sub>2</sub>·6H<sub>2</sub>O, urea, and chitosan in water with the assistance of acetic acid and then dried. After pyrolysis of the sol-gel under N<sub>2</sub> atmosphere, the as-prepared black materials were labeled as the MgO/NC-T catalysts, where T represents the pyrolysis temperature. The Mg content in the MgO/NC-T catalysts gradually increased with the increase of the pyrolysis temperature from 4.6 wt.% at 400 °C to 7.0 wt.% at 600 °C (Table S1) as determined by inductively coupled plasma atomic emission spectroscopy

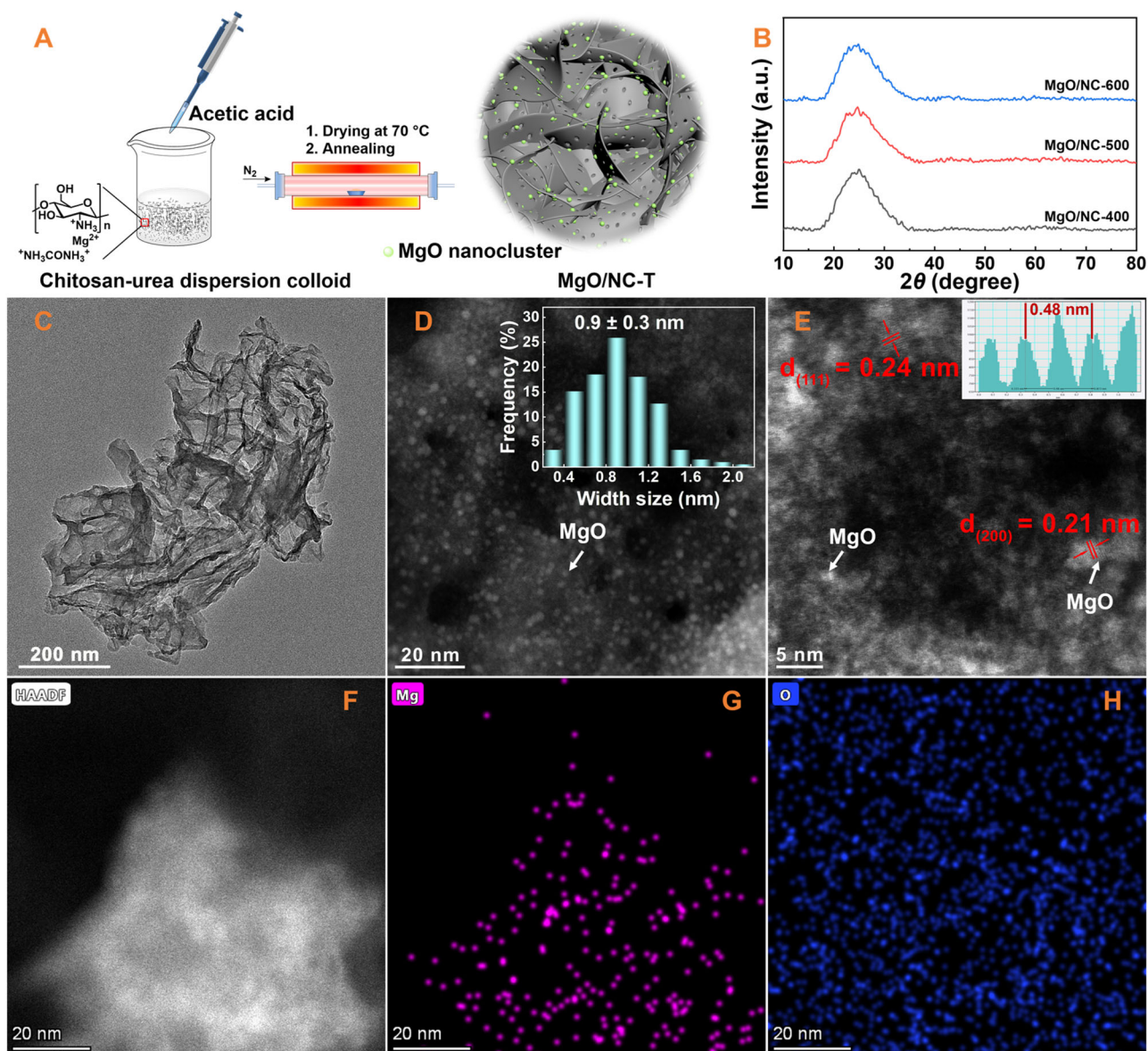


**Fig. 2 | Preparation, XRD, and TEM characterization of the catalysts.** **A** The procedure of the preparation of the MgO/NC-T samples; **B** XRD patterns of the MgO/NC-T samples; **C–E** TEM and AC-HAADF-STEM image (inset: the particle size

distribution of MgO nanoclusters) of MgO/NC-500; **(F–H)** HAADF-STEM image of MgO/NC-500 and corresponding EDS elemental mapping image of Mg and O.

(ICP-AES), due to the release of much more versatile gases at higher pyrolysis temperature. Powder X-ray diffraction (XRD) patterns of MgO/NC-T samples only showed one broad Bragg peak at  $24.4^\circ$  (Fig. 2B), assigning to the (002) crystal plane of graphitic carbon<sup>9,10</sup>. No characteristic peaks related to MgO could be observed in XRD patterns of the MgO/NC-T catalysts, suggesting that MgO in these catalysts may be amorphous or highly dispersed on the nitrogen-doped carbon in small size.

The morphologies of the MgO/NC-T catalysts were further characterized with transmission electron microscopy (TEM). TEM images of the MgO/NC-T catalysts showed a thin-layered structure with no obvious MgO nanoparticles or other Mg species (Fig. 2C and Fig. S1), due to too small particle size and the limited resolution of traditional TEM measurement. Aberration-corrected high-angle annular dark field scanning TEM (AC-HAADF-STEM), which can provide insights into the atomic level structure, was further employed to confirm the presence and state of MgO particles (Fig. 2D). The MgO nanoclusters were

observed as bright spots with a size of  $0.9 \pm 0.3$  nm in the Z-contrast sensitive AC-HAADF-STEM image of MgO/NC-500 (Fig. 2D), indicating that they are likely to be  $(\text{MgO})_4$  nanoclusters, which is the smallest possible neutral  $(\text{MgO})_n$  nanoclusters with the subunit of bulk  $\text{MgO}$ <sup>40</sup>. The lattice fringes of 0.21 nm and 0.24 nm were measured in the AC-HAADF-STEM image of MgO/NC-500 (Fig. 2E), corresponding to the MgO (200) and MgO (111) facets (JCPDS PDF#45-0946). X-ray spectroscopy (EDS) elemental mapping image of MgO/NC-500 further confirmed that Mg homogeneously distributed on nitrogen-doped carbon support with purple spots, and O was found with strong signals at the location of Mg (Fig. 2F, H).

Raman spectroscopy was further employed to study the carbon structure in the MgO/NC-T catalysts (Fig. S2). All of them exhibit two distinct peaks with the Raman shifts around  $1348\text{--}1356\text{ cm}^{-1}$  (D band) and  $1560\text{--}1529\text{ cm}^{-1}$  (G band), representing the graphitic structure and the disordered structure of the MgO/NC-T catalysts, respectively<sup>41</sup>. The intensity ratio of the D band to G band ( $I_D/I_G$ ) was calculated to increase



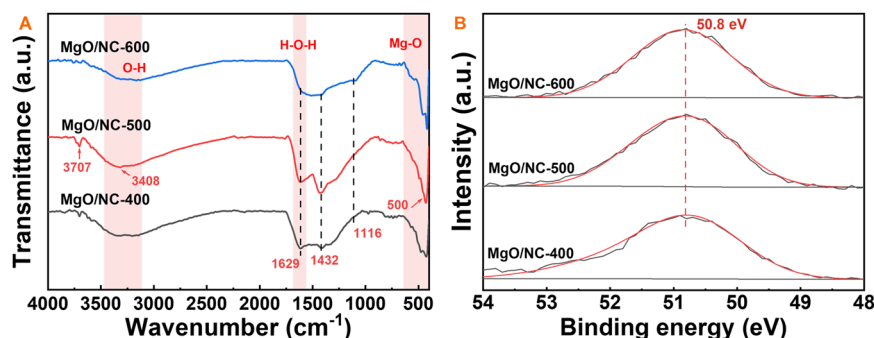


**Fig. 3** | FT-IR and high-resolution Mg 2p XPS spectra of the MgO/NC-T samples. **A** The FT-IR spectra of the MgO/NC-T samples; **B** The high-resolution Mg 2p XPS spectra of the MgO/NC-T samples.

from 1.02 to 1.21 for the MgO/NC-T catalysts with the increase of the pyrolysis temperature from 400 to 600 °C. Furthermore, the structure of the MgO/NC-T catalysts was examined by Fourier-transformed infrared spectroscopy (FT-IR, Fig. 3A). The band at *ca.* 500 cm<sup>-1</sup> was assigned to the bending vibration of  $\nu_{\text{Mg-O}}$ , indicating T<sub>d</sub> symmetry originated from cubic (MgO)<sub>4</sub> nanoclusters<sup>42</sup>. The band at 1116 cm<sup>-1</sup> could be ascribed to the bending vibration of the  $\nu_{\text{C-O}}/\nu_{\text{C-N}}$  from N-doped carbon support, and the band at 1432 cm<sup>-1</sup> was ascribed to the bending vibration of the  $\nu_{\text{C-O}}$ <sup>43</sup>. Two bands at 3408 and 1629 cm<sup>-1</sup> were ascribed to the physically absorbed water-related bending vibration of  $\nu_{\text{O-H}}$  and  $\nu_{\text{H-O-H}}$ , respectively<sup>44,45</sup>. The band at 3707 cm<sup>-1</sup> was observed in the FT-IR spectra of MgO/NC-400 and MgO/NC-500, assigning the stretching vibration of hydroxyl groups in MgO. However, it was too weak to be visible in the FT-IR spectra of MgO/NC-600, suggesting that the surface hydroxyl groups were unstable at high pyrolysis temperatures, e.g. 600 °C<sup>44</sup>.

The chemical environment of the surface elements in the MgO/NC-T catalysts was investigated by X-ray photoelectron spectroscopy (XPS) technology, and core levels of C 1s, N 1s, O 1s, and Mg 2p were recorded (Fig. S3A). The Mg 2p XPS spectra of the MgO/NC-T catalysts showed a main peak with the binding energy at 50.8 eV, corresponding to Mg<sup>2+</sup> in MgO (Fig. 3B)<sup>44,46</sup>. Moreover, the Mg 1s peak with binding energy at 1304.3 eV was also assigned to the Mg<sup>2+</sup> and the low state Mg ions involved with the neighbor trapped electron in F<sup>s+</sup> centers in MgO over these MgO/NC-T catalysts (Fig. S3B)<sup>46</sup>. The N 1s XPS spectra were fitted into four types of nitrogen with binding energies as follows (Fig. S4A–C & Table S2): pyridinic N (398.2 eV), pyrrolic N (399.7 eV), graphitic N (400.7 eV), and oxidized N (401.8 eV)<sup>43</sup>. The peak area percentage of graphitic N was calculated to gradually increase with the increase of the pyrolysis temperatures over the MgO/NC-T catalysts, suggesting that graphitic N was more stable than pyrrolic N and pyridinic N at high temperatures. The C 1s XPS spectra were also fitted and assigned to the following (Fig. S4D–F & Table S3): C–C/C=C (284.6 eV), C–N (285.7 eV), C–O (286.6 eV), C=O (287.8 eV), and O–C=O (289.5 eV)<sup>43</sup>. Four different types of oxygen were fitted in the O 1s XPS spectra of the MgO/NC-T catalysts (Fig. S5 & Table S4), namely O–Mg (530.4 eV), oxygen vacancy (O<sub>v</sub>, 531.4 eV), C=O (532.3 eV) and O–C/O–H (533.6 eV)<sup>43,47,48</sup>. The O 1s peak with the binding energy at 530.4 eV is attributed to the cubic structure of the Mg–O bond in MgO, while the O 1s peak at 531.4 eV corresponds to the O<sub>v</sub> in the small-sized MgO nanoclusters<sup>47,48</sup>.

The presence and the content of O<sub>v</sub> in the *as*-prepared MgO/NC-T catalysts were further determined by electron spin resonance (EPR) spectroscopy. As shown in Fig. 4A, a well-defined signal at *g* = 2.003 was observed in the EPR spectra of the MgO/NC-T catalysts, assigned to O<sub>v</sub><sup>48</sup>. The content of O<sub>v</sub> in the *as*-prepared catalysts greatly increased from MgO/NC-400 to MgO/NC-500, and then decreased for MgO/NC-600. As discussed in the following, O<sub>v</sub> played a crucial role in the adsorption and activation of the substrates. Thus, we also studied the

change in O<sub>v</sub> content after treating the representative MgO/NC-500 catalyst with ethanol or nitrobenzene. As expected, the peak intensity of O<sub>v</sub> significantly decreased after the adsorption of nitrobenzene or ethanol (Fig. 4B), which was due to the fill of negative oxygen atoms in the substrates into the O<sub>v</sub> sites in the MgO/NC-500 catalyst. The nitro group in nitrobenzene is present as the resonance structure with a negatively charged O atom (N<sup>+</sup>–O<sup>-</sup>), and ethanol can generate the ethoxy group (CH<sub>3</sub>CH<sub>2</sub>O<sup>-</sup>) after releasing the H<sup>+</sup> from the –OH group to the basic sites. Thus, these substrates could closely bind with the O<sub>v</sub> sites in the MgO/NC-500 catalyst by filling the negative oxygen atoms in these substrates into O<sub>v</sub> sites. More interestingly, it was noted that the signal of O<sub>v</sub> for the treated sample by ethanol was weaker than that of nitrobenzene, indicating that ethanol had a stronger interaction with O<sub>v</sub> than nitrobenzene.

N<sub>2</sub> adsorption-desorption analysis was also used to evaluate the specific surface areas and pore structures of the MgO/NC-T catalysts (Fig. S6). The isotherm curves of MgO/NC-T samples are identical, showing an IV-type isotherm with an H3 hysteresis loop with no adsorption saturation at higher relative pressure. The presence of an H3 hysteresis loop, commonly observed in layered structures, indicated the formation of mesoporous or microporous materials in the MgO/NC-T catalysts (Table S1). It was noted that both the surface area and pore volume increased with an increase of the pyrolysis temperature, due to the release of much more volatile gases at higher pyrolysis temperatures.

### Catalytic reductive-coupling of nitrobenzene and ethanol

The catalytic performance of the *as*-prepared MgO/NC-T catalysts was screened by the reductive-coupling of nitrobenzene and ethanol at 200 °C. The use of highly inert ethanol as the hydrogen donor for reductive-coupling of nitrobenzene was a very challenging issue and rarely reported, even over noble-metal catalysts. To our pleasure, the *as*-prepared MgO/NC-T catalysts could promote this reductive-coupling reaction, even though they demonstrated different catalytic activity (Table 1, entries 1–3). Besides the presence of the aniline intermediate, the side product of *N*-ethylaniline (**1c**) was not observed over different MgO/NC-T catalysts, suggesting that the further hydrogenation of C = N bonds in *N*-phenylethanamine was completely inhibited over the MgO/NC-T catalysts. Acetal (Table 1, compound 1d), obtained from reversible polycondensation of acetaldehyde and ethanol, instead of acetaldehyde from dehydrogenation of ethanol was detected as the by-product (GC-MS showed in Fig. S7). MgO/NC-500 exhibited the highest catalytic activity with the highest nitrobenzene conversion at 45.6% and the highest TOF value after 6 h (Table 1, entry 2). As stated above, the O<sub>v</sub> sites played a great role in the adsorption and activation of the substrates of ethanol and nitrobenzene for the reductive-coupling reactions. The fact that MgO/NC-500 with the highest O<sub>v</sub> content demonstrated the highest catalytic activity indicated that the O<sub>v</sub> sites should be vital to the reaction. To further

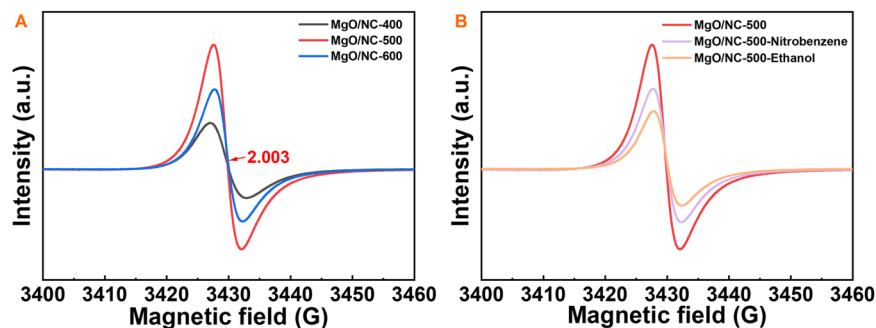


**Fig. 4 | EPR spectra of the samples.** **A** The MgO/NC-T catalysts; **B** The fresh MgO/NC-500 and the treated MgO/NC-500 samples. MgO/NC-500-Nitrobenzene and MgO/NC-500-Ethanol represent the treatment of MgO/NC-500 by nitrobenzene and ethanol.

confirm it, active carbon supported MgO without  $O_v$  (abbreviated as MgO/AC-500) was prepared (see the experimental part for the detail; XRD, EPR, and TEM image shown in Fig. S8 and S1) and tested under identical conditions. Results showed that MgO/AC-500 was nearly inactive (Table 1, entry 4), further confirming the significant role of  $O_v$  in this reductive-coupling reaction. Meanwhile, bulk MgO and NC-500 support were also inactive (Table 1, entries 5 & 6), consistent with the results obtained with the same catalyst loading (Table S5). These results suggested that MgO nanoclusters (Fig. 2D, E), which were abundant in unsaturated coordinated Mg sites and much more surface  $O_v$  sites, were much more active than bulk phase MgO<sup>49,50</sup>.

Some researchers reported that the Mg single-atom catalysts could also be prepared by the same pyrolysis method<sup>51</sup>, and thus the treatment of MgO/NC-500 with HCl to remove MgO nanoclusters was performed to attain MgO free catalyst (abbreviated as Mg<sub>i</sub>/NC-500). Preliminary characterization revealed that MgO nanoclusters were washed off (XRD, FT-IR, and TEM images are provided in Fig. S9), and the atomic Mg spots were observed. Mg<sub>i</sub>/NC-500 delivered negligible activity in the reductive-coupling of nitrobenzene and ethanol (Table 1, entry 7). These results confirmed that MgO nanoclusters with  $O_v$  were the active sites for the reductive-coupling reactions. Interestingly, no *N*-phenylethanamine product was detected using aniline and nitrobenzene/acetaldehyde as the substrates (Table 1, entries 8 and 9). In addition, the dehydrogenation of ethanol was also not observed without nitrobenzene. The same results were obtained using benzyl alcohol as the hydrogen donor, as the product of benzyl alcohol was more easily detected by GC-MS, which also indicates that there were no other by-products of the reaction (Table S6 and GC-MS shown in Fig. S10). These results indicated that the reductive-coupling reaction was a real transfer hydrogenation process in which nitrobenzene served as the H acceptor from alcohols. As far as the transfer hydrogenation of nitrobenzene into aniline, it involves the first hydrogenation of nitrobenzene into nitrosobenzene and the subsequent hydrogenation of nitrosobenzene into aniline. The rapid reactions using nitrosobenzene and aniline/acetaldehyde as substrates indicate that the transfer hydrogenation of nitrobenzene to nitrosobenzene is the rate-limiting step in the reaction process. (Table 1, entries 10 and 11 *vs.* 2).

The reductive-coupling reaction was sensitive to the reaction temperature (Table S7). The reaction almost stopped at 170 °C, and a low conversion of nitrobenzene in 11.7% was attained at 180 °C. Then, the conversion gradually increased with an increase in the reaction temperature. During the reaction process, aniline as the sole intermediate was detected in minor amounts, suggesting that the condensation step of aniline and acetaldehyde was fast. After 28 h, nitrobenzene conversion reached 98.8% at 200 °C with *N*-phenylethanamine in a yield of 93.9% (Fig. S11). The transfer hydrogenation of C = N bonds into *N*-phenylethanamine was still not observed even after a long reaction time (Fig. S11). Besides the high activity and selectivity,

the hot filtration experiment (Fig. S12) and recycling experiments (Fig. S13) both revealed that our prepared MgO/NC-500 catalyst was highly stable during the reaction process due to the strong coordination effect by electron-rich nitrogen atoms in the catalyst. Analysis of hot filtration solution showed that leached Mg after reaction was below the detection limit of ICP-AES (<1.0 µg/L). Therefore, the MgO/NC-500 catalyst was highly stable.

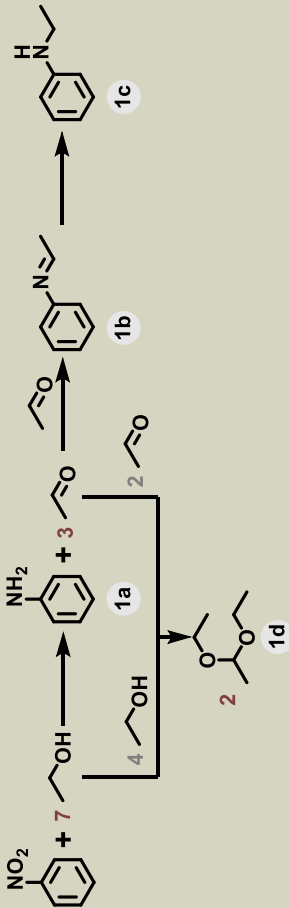
### Substrate scope of the synthesis of organonitrogen chemicals with C = N bonds

The substrate scope of our developed method was studied for the synthesis of representative organonitrogen chemicals with C = N bonds. First, the reductive-coupling of nitro compounds and alcohols was performed for the synthesis of imines. Besides ethanol, other kinds of aliphatic alcohols were also suitable for the reductive-coupling with nitrobenzene, affording the corresponding imines with isolated yields beyond 90% (Fig. 5, entries 1–6). The activity of aliphatic alcohols decreased with an increase in carbon numbers, due to the larger steric hindrance of the aliphatic alcohols with more carbon atoms. Then, different kinds of aromatic/heteroaromatic alcohols were studied for cross-coupling with nitrobenzene in hexane, which was screened to be the optimized reaction solvent (Table S8). The reductive-coupling of nitrobenzene and aromatic/heteroaromatic alcohols also produced the corresponding imines with satisfactory yields (Fig. 5, entries 7–16). Aromatic alcohols with electron-withdrawing groups were slightly more active than those with electron-donating groups (Fig. 5, entries 8, 9 *vs.* 10–12). Heteroaromatic alcohols such as biomass-derived furfural alcohols and 4-pyridinemethanol, which were generally reported to cause the deactivation of metallic nanoparticle catalysts due to the strong affinity of the heteroatoms to the metallic nanoparticles, were also active for the reductive-coupling with nitrobenzene (Fig. 5, entries 13–15). The activity for hetero-aromatic alcohols could be due to the strong interaction between the oxygen atoms in alcohols with the  $O_v$  sites in MgO/NC-500, leading to selective adsorption of the hydroxyl group and avoiding poisoning from heteroatoms on the aromatic ring. Besides primary alcohol, bulky secondary alcohol, 1-phenylethanol, was also effectively coupled with nitrobenzene to generate the corresponding imine with a high yield, but a long reaction time was required (Fig. 5, entries 16 *vs.* 7). Similar steric effect was also observed for *p*-nitrotoluene, *m*-nitrotoluene, and *o*-nitrotoluene (Fig. 5, entries 17 *vs.* 18 & 19).

For the effect of electronic properties of the substituted groups on nitroarenes, it was noted that nitroarenes containing electron-donating groups were more active in the hydrogen transfer coupling with benzyl alcohol than those bearing electron-withdrawing groups (Fig. 5, entries 17–21 *vs.* 22–25). Besides nitroarenes, more challenging cyclic and aliphatic nitro compounds also proceeded smoothly to couple with benzyl alcohol to deliver the corresponding imines with

**Table 1 | Results of the reductive-coupling of nitrobenzene and ethanol<sup>a</sup>**

Entry	Catalyst	Conversion (%)	TOF ( $\mu\text{mol mmol}_{\text{Mg}}^{-1} \text{h}^{-1}$ )	Yield (%)			
				1a	1b	1c	1d
1	MgO/NC-400	15.8	230	5.5	10.3	-	33.6
2	MgO/NC-500	45.6	506	7.7	37.9	-	98.9
3	MgO/NC-600	26.9	256	10.0	16.9	-	56.1
4 <sup>b</sup>	MgO/AC-500	4.0	12	1.7	2.3	-	Trace
5 <sup>b</sup>	MgO	2.5	<1	1.3	1.2	-	-
6 <sup>b</sup>	NC-500	<1	-	Trace	-	-	-
7 <sup>b</sup>	Mg <sub>1</sub> /NC-500	<1	-	Trace	-	-	-
8 <sup>c</sup>	MgO/NC-500	-	-	-	-	-	-
9 <sup>d</sup>	MgO/NC-500	-	-	-	-	-	251.3
10 <sup>e</sup>	MgO/NC-500	>99	-	34.9	63.9	1.2	127.8
11 <sup>f</sup>	MgO/NC-500	>99	-	4.3	95.7	-	194.2



<sup>a</sup>Reaction conditions: nitrobenzene (0.5 mmol), Mg content (25 mg - 40 mg, molar ratio of Mg to nitrobenzene = 0.15:1), 200 °C, ethanol (10 mL), N<sub>2</sub> (10 bar), and 6 h. The conversion and yields were determined by GC with ethylbenzene as the internal standard, and the yield of acetal was obtained based on the amount of nitrobenzene (0.5 mmol) as a reference. <sup>b</sup>The catalyst loading was 100 mg. <sup>c</sup>Aniline (0.5 mmol) was used as substrate. <sup>d</sup>Nitrobenzene (0.5 mmol) and acetaldehyde (3 equiv. corresponding to nitrobenzene) were used as substrates. <sup>e</sup>Nitrobenzene (0.5 mmol) was used as substrate. <sup>f</sup>Aniline (0.5 mmol) and acetaldehyde (3 equiv. corresponding to aniline) were used as substrates.

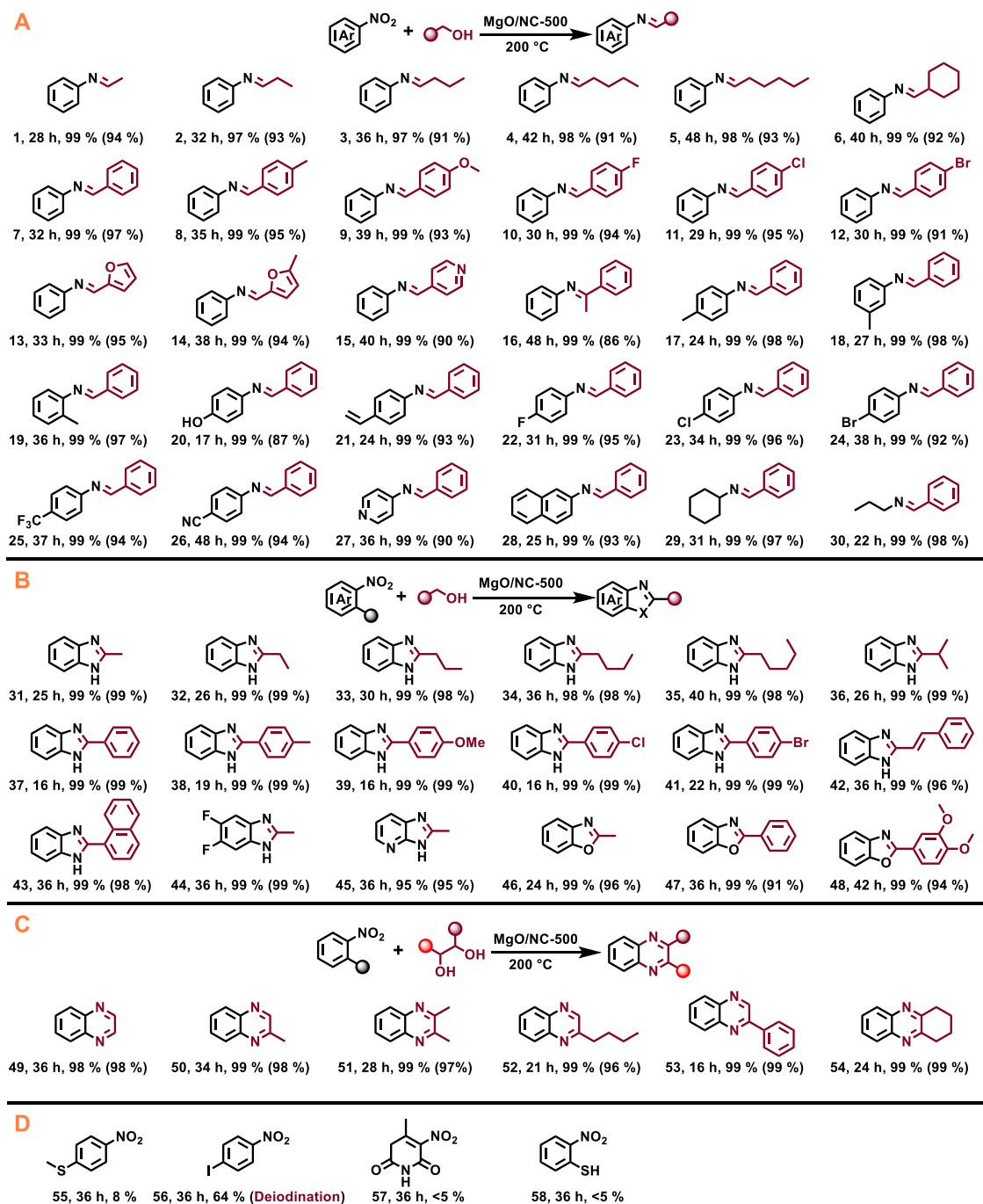


**Fig. 5 | Results of the reductive-coupling of nitro compounds with alcohols.** Reaction conditions: nitro compounds (0.5 mmol), MgO/NC-500 (30.0 mg), aromatic alcohols (2.5 mmol), hexane (10 mL), N<sub>2</sub> (10 bar), and 200 °C; aliphatic alcohols were also used as the reaction solvents when they were used; 10 equiv. of 1, 2-diols were used for the synthesis of quinoxaline. **A** Synthesis of imines;

**B** Synthesis of benzimidazole; **C** Synthesis of quinoxaline; **D** Limitations of nitro compounds. Yields were determined by GC using ethylbenzene as the internal standard, and the data in brackets are the isolated yields. Note: Black balls represent amino or hydroxyl groups on substrate molecules; red and dark red represent alkyl or aryl groups on alcohol molecules.

isolated yields in 90–98% (Fig. 5, entries 27–30). Besides the high catalytic activity, MgO/NC-500 also showed excellent selectivity with good tolerance to many reductive groups such as halogen, nitrile, hydroxyl, and especially vinyl groups (C=C bonds) (Fig. 5, entries 21, 23, 24, and 26), which was one of the most prominent advantages of the MgO/NC-500 catalyst. Great efforts have been devoted to designing effective catalytic systems for the selective hydrogenation of the nitro group without affecting the more thermodynamic- and kinetic-favorable vinyl group, and most of them employed bimetallic

alloys based on high-cost noble metal catalysts<sup>52,53</sup>. This high selectivity for hydrogenation of the nitro group rather than other functional groups such as the vinyl group over MgO/NC-500 could be due to the selective adsorption of the nitro group by the fill of negative oxygen atom in the nitro group to the O<sub>v</sub> sites in MgO nanoclusters, evidenced by EPR experiments (Fig. 4B).

The excellent catalytic performance of MgO/NC-500 towards the synthesis of imines inspired us to further extend our developed method for the synthesis of *N*-heterocycles (Fig. 5, entries 31–54),



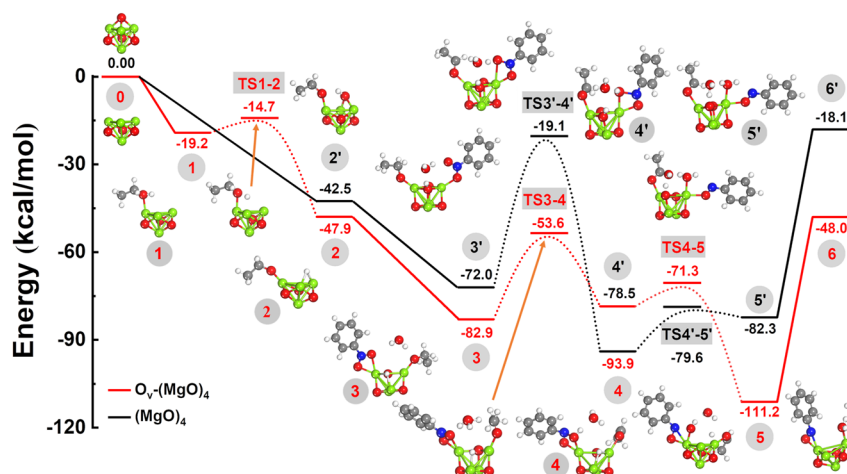


**Fig. 6 | Potential energy profiles of transfer hydrogenation reduction of nitrobenzene to nitrosobenzene by ethanol over the  $(\text{MgO})_4$  and  $\text{O}_v\text{-(MgO)}_4$  surface.** (The red, green, white gray, and blue balls represent O, Mg, H, C, and N atoms, respectively.).

which also proceeded via the reductive-coupling of alcohols with nitro compounds. The reductive-coupling of aliphatic and aromatic alcohols with 2-nitroaniline proceeded smoothly at 200 °C, affording the corresponding 2-substituted benzimidazoles with excellent yields (Fig. 5, entries 31–45). 2-Alkylbenzoxazoles were successfully formed when using 2-nitrophenol as the starting material for the reductive-coupling reactions (Fig. 5, entries 46–48). Besides the formation of benzimidazoles from the reductive-coupling of 2-nitroaniline with primary alcohols,  $\text{MgO/NC-500}$  was also effective for the synthesis of quinoxalines from the reductive-coupling of 2-nitroaniline and 1, 2-diols in high yields (Fig. 5, entries 49–54), which includes the transfer hydrogenation of the nitro group in 2-nitroaniline by 1, 2-diols to generate 1, 2-phenylenediamine and 1, 2-dicarbonyl compounds, followed by the condensation step. The use of main group metal oxide in the reductive coupling of alcohols and nitro compounds for the selective synthesis of organonitrogen chemicals with  $\text{C}=\text{N}$  bonds is demonstrated, exhibiting catalytic performance comparable to or even superior to previously reported systems (Table S9)<sup>9–11,54–56</sup>. However, the sulfur-containing feedstocks and some complex nitro compounds are very difficult or unreactive in the process (Fig. 5, entries 55–58), and for 4-iodonitrobenzene the product underwent deiodination (Fig. 5, entry 56).

### Mechanism study

The above experimental results indicated that the nanocluster-sized  $\text{MgO}$  with abundant  $\text{O}_v$  sites were of great importance for the superior catalytic activity in the reductive-coupling of alcohols and nitro compounds (Table 1 & Fig. 4). The reductive-coupling reaction starts with the adsorption and activating of these substrates (alcohols and nitro compounds) on the  $\text{O}_v$  sites in the  $\text{MgO/NC-500}$  catalyst. DFT calculation was further used to explore the significant role of  $\text{MgO}$  nanoclusters with  $\text{O}_v$  in this reductive-coupling reaction by comparing them with the perfect  $\text{MgO}$ . According to the XRD patterns and AC-HAADF-STEM image of  $\text{MgO/NC-500}$  (Fig. 2), the  $\text{MgO}$  nanocluster [hereinafter referred to as  $(\text{MgO})_4$ ] was utilized as the catalyst model (Fig. S14A). Among different kinds of  $(\text{MgO})_4$  isomers, the energy of cubic isomers was the lowest<sup>40</sup>. DFT calculations revealed that the energy for forming  $\text{O}_v$  in cubic  $\text{MgO}$  nanoclusters [hereinafter referred to as  $\text{O}_v\text{-(MgO)}_4$ ] was 99.7 kcal/mol. Meanwhile, the formation of  $\text{O}_v$  led to decreased valence state of Mg cation in the  $\text{MgO}$  nanoclusters (Fig. S14B).

The difference in the adsorption and activation of ethanol ( $\text{CH}_3\text{CH}_2\text{OH}$ ) molecules between the perfect  $(\text{MgO})_4$  and the  $\text{O}_v\text{-(MgO)}_4$  was first investigated. The adsorption energy ( $E_{\text{ads}}$ ) of ethanol

on  $\text{O}_v\text{-(MgO)}_4$  was calculated to be -19.2 kcal/mol (Fig. 6, 1), and the subsequent H dissociation from -OH group in ethanol requires to overcome an energy barrier ( $E_a$ ) of 4.5 kcal/mol, generating  $\text{-Mg-H}^{6+}$  and  $\text{CH}_3\text{CH}_2\text{O}^-$  species (Fig. 6, TS1-2). However, no energy barrier was required over the perfect  $(\text{MgO})_4$  (Fig. 6, 2'), which could be due to the fact that the Lewis base sites ( $\text{O}^{2-}$  in  $\text{MgO}$ ) promoted ethanol ionization<sup>29,57</sup>. Charge density for ethanol after the adsorption on the  $(\text{MgO})_4$  and  $\text{O}_v\text{-(MgO)}_4$  surfaces was also examined. On  $\text{O}_v\text{-(MgO)}_4$ ,  $\text{Mg}^{2+}$  neighbored to  $\text{O}_v$  donate one electron to  $\text{CH}_3\text{CH}_2\text{OH}$  ( $\sim 0.15$  e<sup>-</sup> transferred to O of ethanol). However, there was no electron transfer between the perfect  $(\text{MgO})_4$  surface and ethanol upon adsorption. Moreover, the length of the  $\alpha\text{-C}_{\text{sp}^3}\text{-H}$  bond in ethanol became longer on the  $\text{O}_v\text{-(MgO)}_4$  surface in comparison with that on the perfect  $(\text{MgO})_4$  surface (1.112 Å *vs.* 1.109 Å), indicating that  $\text{O}_v\text{-(MgO)}_4$  could activate the  $\alpha\text{-C}_{\text{sp}^3}\text{-H}$  bond in ethanol, facilitating the transfer hydrogenation of nitro compounds.

Then, the cleavage of  $\alpha\text{-C}_{\text{sp}^3}\text{-H}$  bond in  $\text{CH}_3\text{CH}_2\text{O}^-$  and the transfer hydrogenation of nitrobenzene on the perfect  $(\text{MgO})_4$  and  $\text{O}_v\text{-(MgO)}_4$  surface was further investigated. As the transfer hydrogenation of nitrobenzene into nitrosobenzene is the rate-determining step in the whole reaction process (Table 1, entries 8, 10 and 11 *vs.* 2), DFT calculation was only performed on this key step. After the dissociation of ethanol into  $\text{CH}_3\text{CH}_2\text{O}^-$  and  $\text{H}^+$  on the perfect  $(\text{MgO})_4$  and  $\text{O}_v\text{-(MgO)}_4$  surface, nitrobenzene could adsorb on the catalyst surface with  $E_{\text{ads}}$  of 29.5 and 35.0 kcal/mol, respectively (Fig. 6, 3 *vs.* 3'). The H atom in  $\alpha\text{-C}_{\text{sp}^3}\text{-H}$  of  $\text{CH}_3\text{CH}_2\text{O}^-$  was then transferred to the "O" atom of the adsorbed nitrobenzene, and the energy barrier for this step was calculated to be 59.0 kcal/mol (Fig. S15). Interestingly, DFT calculation revealed that the energy barrier of the H atom transfer step from  $\alpha\text{-C}_{\text{sp}^3}\text{-H}$  in  $\text{CH}_3\text{CH}_2\text{O}^-$  greatly lowered to 29.3 kcal/mol with the assistance of the  $\text{H}_2\text{O}$  molecule (Fig. 6, TS3-4). Our experimental data also revealed that the addition of a trace amount of water accelerated the reductive-coupling of nitrobenzene with absolute ethanol (Table S10). The improvement of water on the reaction efficiency was also observed by other researchers<sup>58–60</sup>. At the same time, the energy barrier of the transfer of the H atom from  $\alpha\text{-C}_{\text{sp}^3}\text{-H}$  in  $\text{CH}_3\text{CH}_2\text{O}^-$  to the "O" atom of the adsorbed nitrobenzene on the perfect  $(\text{MgO})_4$  was also calculated, and it was much higher than that on the  $\text{O}_v\text{-(MgO)}_4$  surface (52.9 kcal/mol *vs.* 29.3 kcal/mol, Fig. 6, TS3-4 *vs.* TS3'-4'). After the formation of the intermediate with the N-OH bond, it was cleaved to generate the nitrosobenzene intermediate. Meanwhile,  $\text{H}_2\text{O}$  and  $\text{CH}_3\text{CHO}$  (acetaldehyde) were produced on the catalyst surface, desorbed, and the catalyst returned to its initial state (Figs. 6, 4–6). It is worth noting that the generation of water on the  $\text{O}_v\text{-(MgO)}_4$  surface



was more favorable than that on the perfect (MgO)<sub>4</sub> surface (Fig. 6, TS4-5 *vs.* TS4'-5'; 7.2 *vs.* 14.3 kcal/mol) and the subsequent desorption of water on the O<sub>v</sub>-(MgO)<sub>4</sub> surface was also easy (Fig. 6, 5-6 *vs.* 5'-6'; 63.2 kcal/mol *vs.* 64.2 kcal/mol).

As discussed above, the transfer of the H atom from α-C<sub>sp3</sub>-H to the nitro group was much more difficult than the release of the H atom from the -OH group in ethanol. The change of Mulliken charges of Mg<sup>2+</sup> nearby O<sub>v</sub> on the O<sub>v</sub>-(MgO)<sub>4</sub> surface from the adsorption of CH<sub>3</sub>CH<sub>2</sub>O<sup>-</sup> and -O = N<sup>+</sup>-O<sup>-</sup> to the transfer of α-C<sub>sp3</sub>-H was further examined to shed light on this crucial step. Results showed that the Mulliken charges of Mg<sup>2+</sup> changed from +0.607 e<sup>-</sup> to +1.004 - +1.049 e<sup>-</sup> after the adsorption of substrates, revealing that CH<sub>3</sub>CH<sub>2</sub>O<sup>-</sup> and nitrobenzene accepted -0.40 e<sup>-</sup> from Mg<sup>2+</sup> (Fig. S16), which may help activate the α-C<sub>sp3</sub>-H bond in ethanol. The Mulliken charge of Mg<sup>2+</sup> remained at -1.073 e<sup>-</sup> after the direct transfer of the H-atom from the α-C<sub>sp3</sub>-H in CH<sub>3</sub>CH<sub>2</sub>O<sup>-</sup> to the "O" atom in -O = N<sup>+</sup>-O<sup>-</sup>. During the process, the "O" atom in -O = N<sup>+</sup>-O<sup>-</sup> accepted electrons (Mulliken charge changed from -0.421 e<sup>-</sup> to -0.546 e<sup>-</sup>), while the "O" atom in CH<sub>3</sub>CH<sub>2</sub>O<sup>-</sup> loses electrons (Mulliken charge changed from -0.763 e<sup>-</sup> to -0.518 e<sup>-</sup>). The H transfer (from α-C<sub>sp3</sub>-H in CH<sub>3</sub>CH<sub>2</sub>O<sup>-</sup> to -O = N<sup>+</sup>-O<sup>-</sup> in nitrobenzene) was accompanied by the electron transfer from "O" atom in CH<sub>3</sub>CH<sub>2</sub>O<sup>-</sup> to "O" atom in -O = N<sup>+</sup>-O<sup>-</sup> group from nitrobenzene, and Mg<sup>2+</sup> in (MgO)<sub>4</sub> may act as a mediator. Furthermore, the condensation of aniline with acetaldehyde to *N*-phenylethanamine was studied by DFT calculation (Fig. S17). The highest energy barrier (26.5 kcal/mol) for this transformation was lower than the highest energy barrier (29.3 kcal/mol) for the transfer hydrogenation of nitrobenzene to nitrosobenzene (Fig. S17, TS7-8 *vs.* Figure 6, TS3-4), in consistency with experimental data (Table 1, entries 2 *vs.* 10 and 11). Finally, the effect of non-negligible amounts of O species in *N*-doped carbon on activity of MgO clusters supported was investigated. DFT results showed that the addition of oxygen-rich *N*-doped carbon support hardly affected the reaction process and the energy barrier (Fig. S18 *vs.* Fig. 6). Therefore, the support was ignored for the simplification in the DFT calculation. We can conclude that (1) the presence of the O<sub>v</sub> sites promoted the transfer H atoms from α-C<sub>sp3</sub>-H in CH<sub>3</sub>CH<sub>2</sub>O<sup>-</sup> to the nitro group by activating α-C<sub>sp3</sub>-H with longer bond length; (2) Mg<sup>2+</sup> donated electrons to substrates and acts as the electron transfer mediator in the transfer of α-C<sub>sp3</sub>-H in CH<sub>3</sub>CH<sub>2</sub>O<sup>-</sup> to the nitro group, which helped lower the energy barrier in transfer hydrogenations.

Based on the DFT calculation and experimental results, a plausible mechanism was proposed for the reductive-coupling of alcohols and nitro compounds (Fig. 7). Briefly, alcohols and nitro compounds initially adsorb on the O<sub>v</sub> sites in (MgO)<sub>4</sub> nanoclusters. The O-H bond in the adsorbed alcohol molecule is then cleaved, positively charged H on O and an alkoxide group on Mg<sup>2+</sup>. After that, the partially negatively charged H atom from α-C<sub>sp3</sub>-H is transferred to the "O" atom in the nitro group (O = N<sup>+</sup>-O<sup>-</sup>) by the release of one aldehyde molecule, and the active intermediate (O = N-OH) was formed. Then, the cleavage of N-OH bonds delivered nitroso intermediate (-N=O), and the in-situ formed -OH group combines with the H atom in connected with Mg<sup>2+</sup> in (MgO)<sub>4</sub> nanoclusters by the release of one water molecule. After the desorption of aldehyde and water from the surface of the catalyst surface, other cycles for the subsequent transfer of hydrogenation of nitroso intermediate into primary amines proceed in a similar pathway. Finally, the in-situ condensation of primary amines with aldehydes produced the final imine products. As imines with C = N bonds can not generate the stable anionic structure and also have large steric hindrance, the as-formed imines interacted weakly with the O<sub>v</sub> sites in the MgO/NC-500 catalyst, which could fast desorb off from the catalyst surface to avoid further hydrogenation of C = N bonds in imines.

## Discussion

In summary, the nitrogen-doped carbon supported MgO nanoclusters (MgO/NC-500) with abundant oxygen vacancies were

prepared by simple pyrolysis using readily available materials. The MgO/NC-500 catalyst showed excellent performance for the reductive-coupling of alcohols and nitro compounds towards the selective synthesis of imines and *N*-heterocycles with C = N bonds in yields of 86–99%. Our developed method demonstrated advantages including a broad substrate scope with inert aliphatic alcohols, the high selectivity of the organonitrogen chemicals with C = N bonds, and a good tolerance to functional groups. Experimental and theoretical results revealed that the O<sub>v</sub> in MgO nanoclusters selectively adsorbed and activated nitro compounds and alcohols, and the presence of O<sub>v</sub> in MgO nanoclusters greatly lowered the energy barriers in the transfer of the H atoms from alcohols to reduce the nitro groups. Furthermore, the coordinately unsaturated Mg<sup>2+</sup> nearby O<sub>v</sub> mediated the electron transfer between nitro compounds and alcohols. This study provides a solid example of designing earth-abundant and low-cost main group elements based catalysts for some challenging organic transformations as alternatives to traditional transition metal catalysts even noble metal catalysts.

## Methods

### Materials

Magnesium nitrate hexahydrate [Mg(NO<sub>3</sub>)<sub>2</sub>·6H<sub>2</sub>O] and glacial acetic acid (CH<sub>3</sub>COOH, ≥99.5%) were purchased from Sinopharm Chemical Reagent Co., Ltd. (Beijing, China). Urea and chitosan were purchased from Aladdin Chemicals Co. Ltd. (Shanghai, China). All solvents were purchased from Sinopharm Chemical Reagent Co., Ltd. (Shanghai, China). All chemicals used in this study were analytical grade and used without further purification.

### Preparation of the MgO/NC-T catalysts

Typically, urea (12.0 g) and Mg(NO<sub>3</sub>)<sub>2</sub>·6H<sub>2</sub>O (0.6 g) were first dissolved in distilled water (10 mL), and then chitosan (1.0 g) was slowly added into the above solution under vigorous stirring. Glacial acetic acid (1 mL) was quickly added and stirred vigorously for another 30 min to obtain a homogeneous semi-transparent sol-gel. The resulting sol-gel was dried at 70 °C to evaporate water and placed on an alumina boat in a quartz tube furnace, which heated from room temperature to the desired temperature (T) with a ramping rate of 2 °C·min<sup>-1</sup> in a nitrogen atmosphere and then remained at the set temperature for 2 h. After cooling to room temperature, the MgO/NC-T catalysts were obtained as black powder and grounded for further use and characterization.

### Preparation of MgO/AC-500

The activated carbon (AC) supported MgO catalyst (MgO/AC-500) was prepared by loading Mg (NO<sub>3</sub>)<sub>2</sub>·6H<sub>2</sub>O (0.2 g) onto activated carbon (0.3 g) via incipient wet impregnation method and the following calcination at 500 °C under N<sub>2</sub> atmosphere. The Mg loadings in MgO/AC-500 were determined to be 6.3 wt.% by ICP-AES, respectively.

### Catalyst characterizations

Transmission electron microscopy (TEM) images were acquired on a Talos F200X electron microscope at an acceleration voltage of 200 kV. The samples were firstly dispersed in ethanol and dropped onto copper grids for observation. The metal element distribution in the MgO/NC-500 sample was determined by transmission electron microscopy (TEM, FEI Talos F200s electron microscope), aberration-corrected high-annular dark-field scanning TEM (AC HAADF-STEM), and energy-dispersive X-ray spectrometry (EDS). Powder X-ray diffraction (XRD) patterns of the catalysts were recorded on a Bruker advanced D8 powder diffractometer (Cu K<sub>α</sub>). All XRD patterns were collected in the 2θ range of 10–80° with a scanning rate of 0.016 °/s. Surface area and pore size measurements were performed with N<sub>2</sub> adsorption/

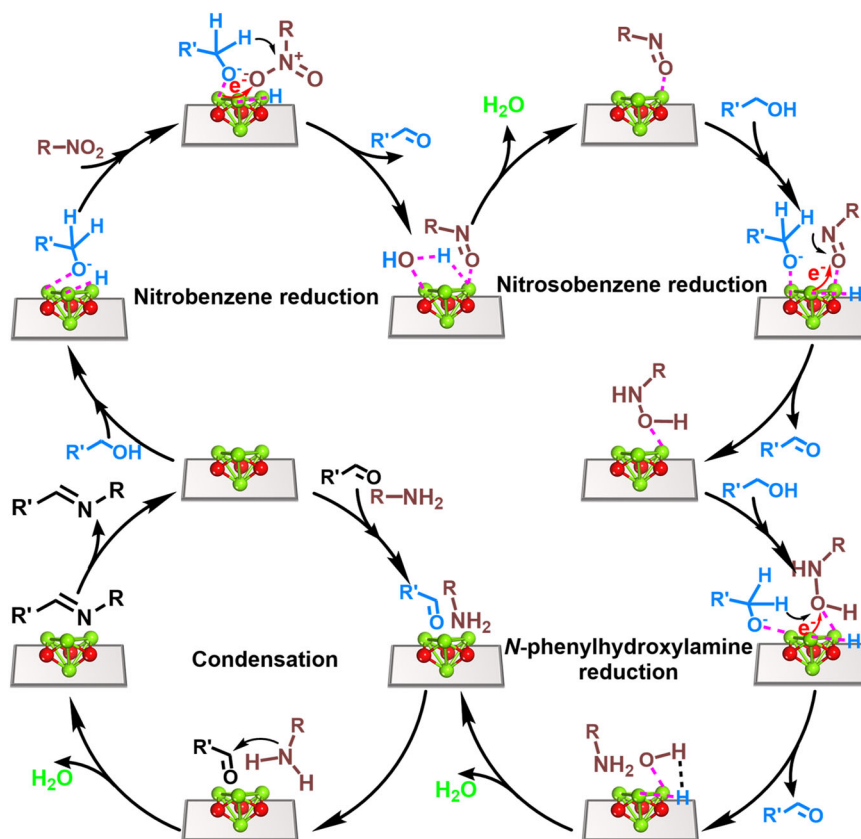


**Fig. 7 | Proposed mechanism for the reductive-coupling of nitro compounds and alcohols over oxygen-defective MgO nanocluster.** (The red, green, white gray, and blue balls represent O, Mg, H, C, and N atoms, respectively.).

desorption isotherms at 77 K on a V-Sorb 2800 P instrument. Before measures, the samples were degassed at 200 °C for 12 h. X-ray photoelectron spectroscopy (XPS) spectra were recorded on a Thermo VG scientific ESCA MultiLab-2000 spectrometer with a monochromatized Al K $\alpha$  source (1486.6 eV) at a constant analyzer pass energy of 25 eV. The binding energy was estimated to be accurate within 0.2 eV. All binding energies were corrected referencing to the C 1s (284.6 eV) peak of the contamination carbon as an internal standard. The Mg content in the catalysts was determined by inductively coupled atomic emission spectrometer (ICP-AES) on an IRIS Intrepid II XSP instrument (Thermo Electron Corporation). Raman spectra were measured on a confocal laser micro-Raman spectrometer (Thermo Fischer DXR) equipped with a diode laser of excitation of 532 nm (laser serial number: AJC1200566). Spectra were obtained at a laser output power of 1 mW (633 nm), and a 0.2 s acquisition time with 900 lines/mm grating (Grating serial number: AJG1200531) in the wavenumber range of 50–3500 cm $^{-1}$ . The electron paramagnetic resonance (EPR) signal was recorded on the Bruker EMXnano EPR spectrometer (Bruker, USA).

### General procedures for the synthesis of imines and *N*-heterocycles

The typical procedure of the synthesis of imines was described as follows: nitrobenzene (0.5 mmol), the MgO/NC-500 catalyst (30 mg), and ethanol (10 mL) were charged into a 40 mL autoclave, which was equipped with a magnetic stirrer, a temperature controller, and a pressure regulator. The air in the autoclave was removed by the flush of N $_2$  for five times, and then the autoclave was charged with 1 MPa N $_2$ . The reaction was then started at 200 °C for 6 h. After cooling to room temperature, the catalyst was collected by centrifugation, and the remaining solvent was subjected to gas chromatography (GC) and GC-mass spectroscopy (GC-MS) analysis.

Procedures for the synthesis of benzazoles (benzimidazoles, benzoxazoles, and benzothiazoles) and quinoxalines were the same as described above using different substrates.

### Analytic methods

Product analysis was performed on an Agilent 7890 A GC instrument with a cross-linked capillary DB-5 column (30 m  $\times$  0.32 mm  $\times$  0.4 mm), which was equipped with a flame ionization detector. N $_2$  was used as the carrier gas with a flow rate of 40 mL min $^{-1}$ . Standard analysis conditions were described as follows: injector temperature 300 °C, detector temperature 300 °C, column temperature program: from 50 °C (hold 1.5 min) to 300 °C (hold 3 min) at a heating rate of 10 °C min $^{-1}$ . The amount of each compound was determined based on the internal standard. The conversion of nitrobenzene ( $Conversion_{Nitrobenzene}$ ), the yield of aniline ( $Yield_{Aniline}$ ), the yield of imine ( $Yield_{Imine}$ ), and the yield of secondary amine ( $Yield_{Secondary amine}$ ) were determined using the Eqs. 1–4 as follows:

$$Conversion_{Nitrobenzene} = \frac{n_{Nitrobenzene} - n'_{Nitrobenzene}}{n_{Nitrobenzene}} \times 100\% \quad (1)$$

$$Yield_{Aniline} = \frac{n_{Produced aniline}}{n_{Nitrobenzene}} \times 100\% \quad (2)$$

$$Yield_{Imine} = \frac{n_{Produced imine}}{n_{Nitrobenzene}} \times 100\% \quad (3)$$

$$Yield_{Secondary amine} = \frac{n_{Produced secondary amine}}{n_{Nitrobenzene}} \times 100\% \quad (4)$$

Where  $n_{\text{Nitrobenzene}}$ ,  $n'_{\text{Nitrobenzene}}$ ,  $n_{\text{Produced aniline}}$ ,  $n_{\text{Produced imine}}$ , and  $n_{\text{Produced secondary amine}}$  represent the initial molar amount of nitrobenzene, the molar amount of nitrobenzene at a certain time, and the molar amount of aniline, imine and secondary amine at a certain time, respectively.

### DFT calculations

All calculations were performed using density functional theory (DFT) under the generalized gradient approximation (GGA) with the Perdew-Burke-Ernzerhof's exchange-correlation functional (PBE) and a spin-polarized scheme as implemented in DMol3 package<sup>61,62</sup>. A double numerical basis set augmented with polarization function (DNP) was employed to describe the electronic structures. Charge analysis was carried out based on the Mulliken population distribution scheme<sup>63</sup>. According to the XRD and aberration-corrected HAADF-STEM results (Fig. 2B, D), the ultra-small MgO catalyst (~0.9 nm) was modeled as a cluster with 4 Mg and 4 O atoms, where the oxygen vacancy was built by removing one O atom in the MgO cluster.

### Recycling experiments

After the reaction, the MgO/NC-500 catalyst was collected by centrifugation, washed with ethanol for three times, and dried in a vacuum for the next use under identical conditions.

### Data availability

The data supporting the findings of this study are available within the article and its Supplementary Information files. All other relevant raw data can be obtained from the corresponding author upon request. Source data are provided with this paper.

### References

- Chandrashekhara, V. G. et al. Nickel-catalyzed hydrogenative coupling of nitriles and amines for general amine synthesis. *Science* **376**, 1433–1441 (2022).
- Ng, X. Q. et al. Direct access to chiral aliphatic amines by catalytic enantioconvergent redox-neutral amination of alcohols. *Nat. Synth.* **2**, 572–580 (2023).
- Afanasyev, O. I. et al. Reductive amination in the synthesis of pharmaceuticals. *Chem. Rev.* **119**, 11857–11911 (2019).
- Njardarson, J. T. *Top 200 small molecule drugs by sales in 2022*. <https://njardarson.lab.arizona.edu/sites/njardarson.lab.arizona.edu/files/NjardarsonGroup2022SmallMoleculeTopPosterV3.pdf>.
- Cui, X. J. et al. Selective acceptorless dehydrogenation of primary amines to imines by core-shell cobalt nanoparticles. *Angew. Chem. Int. Ed.* **59**, 7501–7507 (2020).
- Murugesan, K. et al. Catalytic reductive aminations using molecular hydrogen for synthesis of different kinds of amines. *Chem. Soc. Rev.* **49**, 6273–6328 (2020).
- Borthakur, I. et al. Reductive alkylation of azides and nitroarenes with alcohols: A selective route to mono- and dialkylated amines. *J. Org. Chem.* **87**, 628–643 (2021).
- Liu, M. T. et al. Enhancing reductive C–N coupling of nitro compounds through interfacial engineering of MoO<sub>3</sub> in thin carbon layers. *Chem. Commun.* **59**, 12443–12446 (2023).
- Liu, D. et al. Direct reductive coupling of nitroarenes and alcohols catalysed by Co–N–C/CNT@AC. *Green. Chem.* **21**, 2129–2137 (2019).
- Wu, C. et al. Nano-pyramid-type Co–ZnO/NC for hydrogen transfer cascade reaction between alcohols and nitrobenzene. *Appl. Catal. B-Environ.* **300**, 120288 (2022).
- Li, W. K. et al. Enhanced hydride donation achieved molybdenum catalyzed direct N-alkylation of anilines or nitroarenes with alcohols: From computational design to experiment. *ACS Catal.* **11**, 10377–10382 (2021).
- Shen, X. J. et al. Catalytic self-transfer hydrogenolysis of lignin with endogenous hydrogen: Road to the carbon-neutral future. *Chem. Soc. Rev.* **51**, 1608–1628 (2022).
- Wang, T. et al. Identification of active catalysts for the acceptorless dehydrogenation of alcohols to carbonyls. *Nat. Commun.* **12**, 5100 (2021).
- Wang, Y. L. et al. A new paradigm in pincer iridium chemistry: PCN complexes for (de) hydrogenation catalysis and beyond. *Acc. Chem. Res.* **55**, 2148–2161 (2022).
- Xiong, N. et al. Mild amide synthesis using nitrobenzene under neutral conditions. *Org. Lett.* **24**, 4766–4771 (2022).
- Su, H. et al. Grouping effect of single Nickel–N<sub>4</sub> sites in nitrogen-doped carbon boosts hydrogen transfer coupling of alcohols and amines. *Angew. Chem. Int. Ed.* **57**, 15194–15198 (2018).
- Chen, Z. W. et al. Construction Co–ZnO acid-base pair catalysts for alcohol and nitrobenzene hydrogen transfer cascade reaction. *Appl. Catal. B-Environ.* **340**, 123203 (2024).
- Chandrashekhara, V. G. et al. Silica-supported Fe/Fe–O nanoparticles for the catalytic hydrogenation of nitriles to amines in the presence of aluminium additives. *Nat. Catal.* **5**, 20–29 (2022).
- Goulas, K. A. et al. Fundamentals of C–O bond activation on metal oxide catalysts. *Nat. Catal.* **2**, 269–276 (2019).
- Yuan, Z. L. et al. Synergy of oxygen vacancies and base sites for transfer hydrogenation of nitroarenes on ceria nanorods. *Angew. Chem. Int. Ed.* **63**, e202317339 (2024).
- Hayashi, E. et al. Effect of MnO<sub>2</sub> crystal structure on aerobic oxidation of 5-hydroxymethylfurfural to 2, 5-furandicarboxylic acid. *J. Am. Chem. Soc.* **141**, 890–900 (2019).
- Liu, D. L. et al. Understanding the nature of ammonia treatment to synthesize oxygen vacancy-enriched transition metal oxides. *Chem* **5**, 376–389 (2019).
- Wang, H. et al. Strong metal-support interactions on gold nanoparticle catalysts achieved through Le Chatelier's principle. *Nat. Catal.* **4**, 418–424 (2021).
- Xu, Q. et al. Al<sup>3+</sup> dopants induced Mg<sup>2+</sup> vacancies stabilizing single-atom Cu catalyst for efficient free-radical hydrophosphinylation of alkenes. *J. Am. Chem. Soc.* **144**, 4321–4326 (2022).
- Wang, Q. Y. et al. Atomically dispersed s-block magnesium sites for electroreduction of CO<sub>2</sub> to CO. *Angew. Chem. Int. Ed.* **60**, 25241–25245 (2021).
- Shao, X. B. et al. Magnesium single-atom catalysts with super-basicity. *Sci. China Chem.* **66**, 1737–1743 (2023).
- Liang, Y. Y. et al. Magnesium pincer complexes and their applications in catalytic semihydrogenation of alkynes and hydrogenation of alkenes: Evidence for metal-ligand cooperation. *J. Am. Chem. Soc.* **144**, 19115–19126 (2022).
- Liang, Y. Y. et al. Designing new magnesium pincer complexes for catalytic hydrogenation of imines and N-heteroarenes: H<sub>2</sub> and N–H activation by metal-ligand cooperation as key steps. *J. Am. Chem. Soc.* **145**, 9164–9175 (2023).
- de Souza, E. F. et al. Computational and experimental mechanistic insights into the ethanol-to-butanol upgrading reaction over MgO. *ACS Catal.* **10**, 15162–15177 (2020).
- Liu, P. X. et al. Atomically dispersed iridium on MgO (111) nanosheets catalyzes benzene-ethylene coupling towards styrene. *Nat. Catal.* **4**, 968–975 (2021).
- Eppele, M. et al. The why and how of ultrasmall nanoparticles. *Acc. Chem. Res.* **56**, 3369–3378 (2023).
- Chen, S. J. et al. Ultrasmall amorphous zirconia nanoparticles catalyze polyolefin hydrogenolysis. *Nat. Catal.* **6**, 161–173 (2023).
- Hao, X. D. et al. Atomic-scale valence state distribution inside ultrafine CeO<sub>2</sub> nanocubes and its size dependence. *Small* **14**, 1802915 (2018).



34. Wang, Q. et al. Oxygen vacancies boosted fast  $\text{Mg}^{2+}$  migration in solids at room temperature. *Energy Stor. Mater.* **51**, 630–637 (2022).
35. Mofarah, S. S. et al. Proton-assisted creation of controllable volumetric oxygen vacancies in ultrathin  $\text{CeO}_{2-x}$  for pseudocapacitive energy storage applications. *Nat. Commun.* **10**, 2594 (2019).
36. Hao, Y. N. et al. MXene-regulated metal-oxide interfaces with modified intermediate configurations realizing nearly 100%  $\text{CO}_2$  electrocatalytic conversion. *Angew. Chem. Int. Ed.* **62**, e202304179 (2023).
37. Xu, S. et al. Selective oxidation of 5-hydroxymethylfurfural to 2,5-furandicarboxylic acid using  $\text{O}_2$  and a photocatalyst of Co-thiophenopyrazine bonded to  $\text{g-C}_3\text{N}_4$ . *J. Am. Chem. Soc.* **139**, 14775–14782 (2017).
38. Xie, C. et al. Zn- $\text{N}_x$  sites on N-doped carbon for aerobic oxidative cleavage and esterification of C(CO)-C bonds. *Nat. Commun.* **12**, 4823 (2021).
39. Fiorio, J. L. et al. Recent advances in the use of nitrogen-doped carbon materials for the design of noble metal catalysts. *Coord. Chem. Rev.* **481**, 215053 (2023).
40. Chen, M., Felmy, A. R. & Dixon, D. A. Structures and stabilities of  $(\text{MgO})_n$  nanoclusters. *J. Phys. Chem. A* **118**, 3136–3146 (2014).
41. Ferrari, A. C. & Basko, D. M. Raman spectroscopy as a versatile tool for studying the properties of graphene. *Nat. Nanotechnol.* **8**, 235–246 (2013).
42. Haertelt, M. et al. Structure determination of neutral MgO clusters-hexagonal nanotubes and cages. *Phys. Chem. Chem. Phys.* **14**, 2849–2856 (2012).
43. Li, X. et al. Nitrogen-doped carbon as a highly active metal-free catalyst for the selective oxidative dehydrogenation of *N*-heterocycles. *ChemSusChem* **15**, e202200753 (2022).
44. Gao, P. P. et al. Fabrication, performance and mechanism of MgO meso-/macroporous nanostructures for simultaneous removal of As (III) and F in a groundwater system. *Environ. Sci.-Nano* **3**, 1416–1424 (2016).
45. Finocchi, F. & Goniakowski, J. Interaction of a water molecule with the oxygen vacancy on the MgO (100) surface. *Phys. Rev. B* **64**, 125426 (2001).
46. Hao, Y. J. et al. Synthesis of {111} facet-exposed MgO with surface oxygen vacancies for reactive oxygen species generation in the dark. *ACS Appl. Mater. Interfaces* **9**, 12687–12693 (2017).
47. Cao, N. W. et al. Superior selective adsorption of MgO with abundant oxygen vacancies to removal and recycle reactive dyes. *Sep. Purif. Technol.* **275**, 119236 (2021).
48. Su, X. J. et al. The enhanced photocatalytic performance of the amorphous carbon/MgO nanofibers: Insight into the role of the oxygen vacancies and 1D morphology. *Appl. Surf. Sci.* **616**, 156470 (2023).
49. Deshpande, S. et al. Size dependency variation in lattice parameter and valency states in nanocrystalline cerium oxide. *Appl. Phys. Lett.* **87**, 133113 (2005).
50. Xu, J. H. et al. Size dependent oxygen buffering capacity of ceria nanocrystals. *Chem. Commun.* **46**, 1887–1889 (2010).
51. Liu, S. et al. Turning main-group element magnesium into a highly active electrocatalyst for oxygen reduction reaction. *Nat. Commun.* **11**, 938 (2020).
52. Liu, W. et al. Highly-efficient RuNi single-atom alloy catalysts toward chemoselective hydrogenation of nitroarenes. *Nat. Commun.* **13**, 3188 (2022).
53. Nakaya, Y. & Furukawa, S. Catalysis of alloys: Classification, principles, and design for a variety of materials and reactions. *Chem. Rev.* **123**, 5859–5947 (2022).
54. Sabater, S., Mata, J. A. & Peris, E. Dual catalysis with an  $\text{Ir}^{\text{III}}$ -Au<sup>I</sup> heterodimetallic complex: Reduction of nitroarenes by transfer hydrogenation using primary alcohols. *Chem. Eur. J.* **18**, 6380–6385 (2012).
55. Daw, P. et al. Synthesis of pyrazines and quinoxalines via acceptorless dehydrogenative coupling routes catalyzed by manganese pincer complexes. *ACS Catal.* **8**, 7734–7741 (2018).
56. Wu, J. & Darcel, C. Iron-catalyzed hydrogen transfer reduction of nitroarenes with alcohols: Synthesis of imines and aza heterocycles. *J. Org. Chem.* **86**, 1023–1036 (2020).
57. Lu, B. et al. Efficient conversion of ethanol to 1-butanol over adjacent acid-base dual sites via enhanced C-H activation. *ACS Catal.* **13**, 4866–4872 (2023).
58. Liu, S. Z., White, M. G. & Liu, P. Mechanism of oxygen reduction reaction on Pt (111) in alkaline solution: Importance of chemisorbed water on surface. *J. Phys. Chem. C* **120**, 15288–15298 (2016).
59. Ma, X. T. et al. DFT study of  $\text{CO}_2$  adsorption across a  $\text{CaO}/\text{Ca}_{12}\text{Al}_{14}\text{O}_{33}$  sorbent in the presence of  $\text{H}_2\text{O}$  under calcium looping conditions. *Chem. Eng. J.* **370**, 10–18 (2019).
60. Zhao, S. et al. Remarkable active-site dependent  $\text{H}_2\text{O}$  promoting effect in CO oxidation. *Nat. Commun.* **10**, 3824 (2019).
61. Perdew, J. P., Burke, K. & Ernzerhof, M. Generalized gradient approximation made simple. *Phys. Rev. Lett.* **77**, 3865–3868 (1996).
62. Delley, B. From molecules to solids with the DMol3 approach. *J. Chem. Phys.* **113**, 7756–7764 (2000).
63. Mulliken, R. S. Electronic population analysis on LCAO-MO molecular wave functions. IV. Bonding and antibonding in LCAO and valence-bond theories. *J. Chem. Phys.* **23**, 2343–2346 (1955).

## Acknowledgements

The authors thank the support of the Project were Supported by the National Key Research and Development Program of China (2024YFE0203000) and the National Natural Science Foundation of China (22479165 and 22179148).

## Author contributions

Z.L.Y. conducted the experiments and discussed the work. Z.L.Y., B. L., P.Z., J. Sun, R.T.M. and Z.H.Z. conceived the work, designed the experiments, and analyzed the data; B.H. performed and supervised the DFT calculations; Z.H.Z. supervised the whole project. All the authors discussed the results and were involved in the writing of the manuscript.

## Competing interests

The authors declare no competing interests.

## Additional information

**Supplementary information** The online version contains supplementary material available at <https://doi.org/10.1038/s41467-025-58222-6>.

**Correspondence** and requests for materials should be addressed to Jie Sun, Rentao Mu or Zehui Zhang.

**Peer review information** *Nature Communications* thanks Kuo-Wei Huang and the other, anonymous, reviewer(s) for their contribution to the peer review of this work. A peer review file is available.

**Reprints and permissions information** is available at <http://www.nature.com/reprints>

**Publisher's note** Springer Nature remains neutral with regard to jurisdictional claims in published maps and institutional affiliations.



**Open Access** This article is licensed under a Creative Commons Attribution-NonCommercial-NoDerivatives 4.0 International License, which permits any non-commercial use, sharing, distribution and reproduction in any medium or format, as long as you give appropriate credit to the original author(s) and the source, provide a link to the Creative Commons licence, and indicate if you modified the licensed material. You do not have permission under this licence to share adapted material derived from this article or parts of it. The images or other third party material in this article are included in the article's Creative Commons licence, unless indicated otherwise in a credit line to the material. If material is not included in the article's Creative Commons licence and your intended use is not permitted by statutory regulation or exceeds the permitted use, you will need to obtain permission directly from the copyright holder. To view a copy of this licence, visit <http://creativecommons.org/licenses/by-nc-nd/4.0/>.

© The Author(s) 2025